Supplementary material

Sojiro Fukuda[1*], Marijke G. W. de Vet[1], Edward W. G. Skevington[1], Elena Bastianon[1], Roberto Fernández[1], Xuxu Wu[1], William D. McCaffrey[2], Hajime Naruse[3], Daniel R. Parsons[1], and Robert M. Dorrell[1]

[1]Energy and Environment Institute, University of Hull, Hull, United Kingdom
[2]School of Earth and Environment, University of Leeds, Leeds, United Kingdom
[3]Department of Geology and Mineralogy, Division of Earth and Planetary Sciences, Graduate School of Science, Kyoto University, Kyoto, Japan
[*]e-mail: S.Fukuda-2018@hull.ac.uk

Non-dimensional flow characterization

Here the quasi-equilibrium flow condition is assumed, where the mean flow parameters do not vary in time and space but the turbulent fluctuation from mean flow parameters are still present. To describe these flow states, coordinate systems, and flow characteristics are introduced in this section. $\mathbf{x} = (x, y, z)$ denotes the spatial coordinate of the given point, where x is the streamwise direction, y is the lateral direction, and z is the bed-normal direction ($z = 0$ at the bed). Flow velocity is denoted by $\mathbf{u}(\mathbf{x},t) = (u, v, w)$. Volumetric flow concentration at a given height is denoted by $\phi(z)$. Reynolds averages[1] are introduced here to describe the mean flow characteristics and their fluctuations as follows

$$u(\mathbf{x},t) = \langle u(\mathbf{x},t)\rangle + u'(\mathbf{x},t), \;\; v(\mathbf{x},t) = \langle v(\mathbf{x},t)\rangle + v'(\mathbf{x},t), \tag{S.1}$$

$$w(\mathbf{x},t) = \langle w(\mathbf{x},t)\rangle + w'(\mathbf{x},t), \;\; \phi(\mathbf{x},t) = \langle \phi(\mathbf{x},t)\rangle + \phi'(\mathbf{x},t). \tag{S.2}$$

where $\langle\cdot\rangle$ denotes the temporal Reynolds average and primes denote the Reynolds fluctuations ($\langle u'\rangle = \langle v'\rangle = \langle w'\rangle = \langle \phi'\rangle = 0$). Then, the mean-flow field of quasi-equilibrium turbidity current is defined by introducing depth-averaged parameters as follows

$$U = \frac{1}{h(x)}\int_0^\infty \langle u(\mathbf{x})\rangle \mathrm{d}z, \;\; V = \frac{1}{h(x)}\int_0^\infty \langle v(\mathbf{x})\rangle \mathrm{d}z, \;\; W = \frac{1}{h(x)}\int_0^\infty \langle w(\mathbf{x})\rangle \mathrm{d}z, \;\; \Phi = \frac{1}{h(x)}\int_0^\infty \langle \phi(\mathbf{x})\rangle \mathrm{d}z, \tag{S.3}$$

where $h(x)$ denotes flow depth. It should be noted that it is assumed that flow parameters do not vary in time for quasi-equilibrium turbidity currents. Flow depth is defined as the height at which both flow velocity and concentration vanish, which is

$$h(x) = \max\left[z|_{\langle u\rangle=0}, z|_{\langle \phi\rangle=0}\right], \tag{S.4}$$

where $z|_{\langle u\rangle=0}$ is the flow depth above which flow velocity becomes negligible and $z|_{\langle \phi\rangle=0}$ is the flow depth above which concentration difference between the floa and the ambient fluid becomes negligible. In the ideal condition, $z|_{\langle u\rangle=0} = z|_{\langle \phi\rangle=0}$. However, in the actual measurement of experiments, $z|_{\langle u\rangle=0}$ is not always the same value as $z|_{\langle \phi\rangle=0}$ for various reasons such as i) the effects of the non-zero flow velocity of ambient fluid, ii) the error of velocity or density measurements at the upper layer of the flow, and iii) error due to the extrapolation methodology. In particular, the vertical gradient of a concentration profile of turbidity currents tends to be very small and show gradual transition to ambient fluid. Thus, measurement error near the upper boundary could cause a significant error of the estimation of $z|_{\langle \phi\rangle=0}$. The majority of flume experiments use a few to a dozen siphon tubes to measure the flow concentration. On the other hand, the majority of compiled experiments measured vertical velocity profiles by using UVP or ADV, which have a much higher resolution than a siphon array. However, some of the flume experiments also have low resolution of velocity profiles, such as Michon et al.[2], Altinakar et al.,[3] and Tesaker[4] (Table S1). Thus, the accuracy of $z|_{\langle u\rangle=0}$ and $z|_{\langle \phi\rangle=0}$ varies between each experiment. In this study, the zero-velocity and zero-concentration heights are carefully compared, and the more reliable one was employed as flow depth (see below for detailed procedures).

To describe the flow state, the following non-dimensional flow parameters are introduced. Firstly, the Richardson number, *Ri* the ratio of the buoyancy and the flow shear stress, is given as,

$$\mathrm{Ri} = \frac{-g(\partial\rho/\partial z)}{\rho'(\partial\langle u\rangle/\partial z)^2} \simeq \frac{g\Delta\rho/h}{\rho' U^2/h^2} = \frac{gR\Phi h}{U^2} \tag{S.5}$$

where ρ is the flow density, ρ' is the density of the ambient fluid, and $\Delta\rho$ is the density difference between the flow and the ambient fluid ($\rho - \rho'$). The shear velocity, u_*, is calculated using the logarithmic law local to the bed,

$$\frac{\mathrm{d}\langle u\rangle}{\mathrm{d}z} = \frac{u_*}{\kappa z} \tag{S.6}$$

The skin drag coefficient, C_D, is defined as

$$C_\mathrm{D} = \frac{u_*^2}{U^2}. \tag{S.7}$$

In this study, the particle settling velocity, w_s, for relatively coarse material (> 100μm) is prescribed by an empirical formula covering a combined viscous plus bluff-body drag law for natural irregular sand grains[5],

$$w_\mathrm{s} = \frac{\nu}{d_{50}}\left[(10.36^2 + 1.049D_\mathrm{s}^3)^{\frac{1}{2}} - 10.36\right]. \tag{S.8}$$

where d_{50} is the median grain size, and $D_\mathrm{s} = (g\Delta\rho/\rho\nu^2)^{1/3}d_{50}$ is the dimensionless particle diameter, ν is the fluid viscosity. For the finer particles (< 100μm), Stokes' law is applied,

$$w_\mathrm{s} = \frac{Rgd_{50}^2}{C_1\nu} \tag{S.9}$$

where R is specific gravity and C_1 is a constant with a theoretical value of 18.

Data compilation

The compiled published sources are listed in Table S1. In total, 19 laboratory-experiments, 1 numerical simulation, and 1 direct-observation source were gathered. Since each source uses different tools for vertical-profile measurement, the data are compiled carefully. For example, the velocity measurement of flume experiments can be categorized into 5 different types: micro-propeller current-meters, velocity meters, UVPs (Ultrasonic Velocity Profiler), ADVs (Acoustic Doppler Velocity probes). For both UVPs and ADVs, each source used a different number of probes, sampling rate, and angle of mounting. The vertical flow profiles reported in each source are based on interpolation and extrapolation, the methods differing between the sources. To perform consistent analysis, here, only the original measurement points are extracted from each sources to minimize the errors. Then, a consistent interpolation and extrapolation method are applied to recover the full vertical profiles.

Particle-size distribution analyses The potential error of particle size due to the different particle-size analyses are carefully considered. Settling velocity, w_s, plays an important role in the required work done to keep sediment in suspension, $B = gR\Phi hw_s$. The particle-size analysis methods in the compiled source in this study are either sieving combined with hydrometer method (SHM) or the laser diffraction method (LDM). SHM measures the settling velocity of the particles in a liquid. In SHM, the particles are assumed to be spherical and their sizes are calculated based on Stokes' law[23]. On the other hand, in LDM, the measured particles size becomes equivalent to that of a sphere giving the same diffraction as the particles. LDM can process each sample faster and provide more detailed information such as the number of particles and surface area, compared with SHM[24]. Further, LDM provides high repeatability and reproducibility[25].

Extensive comparison of SHM and LDM[24,26–32] has shown a large discrepancy between the measured proportion of clay-size particles. Although the discrepancy becomes negligible for sand-size particles in most cases, when comparing the size of the largest particles in sample of silt to clay-size particles, the error can be up to two orders of magnitude[29]. The particle-size error of two orders of magnitude can result in up to 4 order of magnitude errors of settling velocity (Eq.(S.9)). Those measurement discrepancies are attributed to the density difference and shape variation of particles[33].

In this study, particle size distribution from LDS is regarded as more reliable data than the SHM. Tesaker's experiment[4] used SHM to measure the particle size distribution of their clay material, and the reported median particle size varies between 0.8–2.3 microns of which particle-size range is likely to be significantly underestimated. To mitigate this systematic error due to the difference of methodology, in this study, the following modification of reported particle size is conducted.

Firstly, cumulative particle distribution curves of similar materials as Tesaker's experiments (Kaolinite clay) are extracted from the particle-size comparison studies between SHM and LDM[30,31]. Since the particle-size discrepancy between SHM and LDM could show different trends based on the type of clay minerals, only the datasets in which material is mainly composed of Kaolinite were chosen. The cumulative particle distribution curve, $F(d_i)$ is defined as in

$$F(d_i) = \sum_{k=0}^{i} f(d_k) \tag{S.10}$$

source	TYPE	Slope (%)	Material	d_{50} (μm)	Measurement tools
Michon et al.[2]	II	0.3–3.6	Kaolinite	14.6	$\langle u \rangle$: MPCM $\langle \phi \rangle$: Siphon array (4–12)
Tesaker[4]	II	5.0–12.5	Quartz Kaolinite	360–410 1.1–1.5^{*4}	$\langle u \rangle$: Velocity meters^{*6}(3) $\langle \phi \rangle$: Siphon array (3)
Altinakar[3]	II	1.0–2.96	Quartz Salt	14 / 32 –	$\langle u \rangle$: MPCM $\langle \phi \rangle$: Siphon array (16)
Garcìa[6]	II	8	Silica	9	$\langle u \rangle$: MPCM $\langle \phi \rangle$: Optical probes
Packman & Jerolmack[7]	II	1.0	Quartz Kaolinite	12 1.3	$\langle u \rangle$: ADV $\langle \phi \rangle$: Siphon array (6)
Amy et al.[8]	II	5.2	Glycerol	–	$\langle u \rangle$: UVP array (8) $\langle \phi \rangle$: Siphon array (5)
Islam and Imran[9]	II & III	0.0-8.0	Silt / Salt	25	$\langle u \rangle$: ADV $\langle \phi \rangle$: Siphon array (20)
Sequeiros et al.[10]	II	0.85–5.0	Salt^{*3}	–	$\langle u \rangle$: ADV $\langle \phi \rangle$: Siphon array (10)
Sequeiros et al.[11]	II	5.0	Salt^{*3}	–	$\langle u \rangle$: ADV $\langle \phi \rangle$: Siphon array (10)
Cartigny et al.[12]	III	12.3–21.3	Quartz	160	$\langle u \rangle$: Angled UVP $\langle \phi \rangle$: –
Fedele et al.[13]	II	8.7–17.6	Salt	–	$\langle u \rangle$: ADV $\langle \phi \rangle$: Siphon array (20)
Leeuw et al.[14]	II & III	15.8–19.4	Sand	141	$\langle u \rangle$: Angled UVP $\langle \phi \rangle$: Siphon array (4)
Leeuw et al.[15]	III	19.4	Sand	131	$\langle u \rangle$: Angled UVP $\langle \phi \rangle$: –
Hermidas et al.[16]	III	10.5–16.7	Quartz Kaolinite	150/46 0.18	$\langle u \rangle$: Angled UVP $\langle \phi \rangle$: –
Sequeiros et al.[17]	II	9.0	Plastic	57	$\langle u \rangle$: Angled UVP $\langle \phi \rangle$: Siphon array (11)
Eggenhuisen et al.[18]	II	7.0–14.0	Sand	130	$\langle u \rangle$: Angled UVP $\langle \phi \rangle$: Siphon array (4)
Kelly et al.[19]	II^{*1} & III	3.5	Salt	– –	$\langle u \rangle$: ADV $\langle \phi \rangle$: –
Koller et al.[20]	II^{*2}	0.9–2.6	Salt	–	$\langle u \rangle$: UVP array (10) $\langle \phi \rangle$: Siphon array (6)
Pohl et al.[21]	II	14.1	Quartz	133	$\langle u \rangle$: Angled UVP $\langle \phi \rangle$: Siphon array (4)
Simmons et al.[22]	I	0.7	Silt	9.9–11^{*5}	$\langle u \rangle$: ADCPs $\langle \phi \rangle$: ADCPs

MPCM: Micro-Propeller Current-Meter; UVP: Ultrasonic Velocity Profiler;
ADV: Acoustic Doppler Profiler; ADCPs: Acoustic Doppler Current Profilers

Table S1. Summary of compiled source. The figures in the parentheses represent the number of equipment in the array. ^{*1} Numerical simulation of Reynolds-averaged Navier-Stokes model. ^{*2} Limited information of concentration profiles to use in this study. ^{*3} There are also experiments with sediment in the source, but the availability of flow profiles is limited. ^{*4} Original reported values of particle size from hydrometer analysis. ^{*5} d_{50} from Event 1, 4, and 5 from the original source. ^{*6} Velocity meters are special equipment that are designed for their particular study.

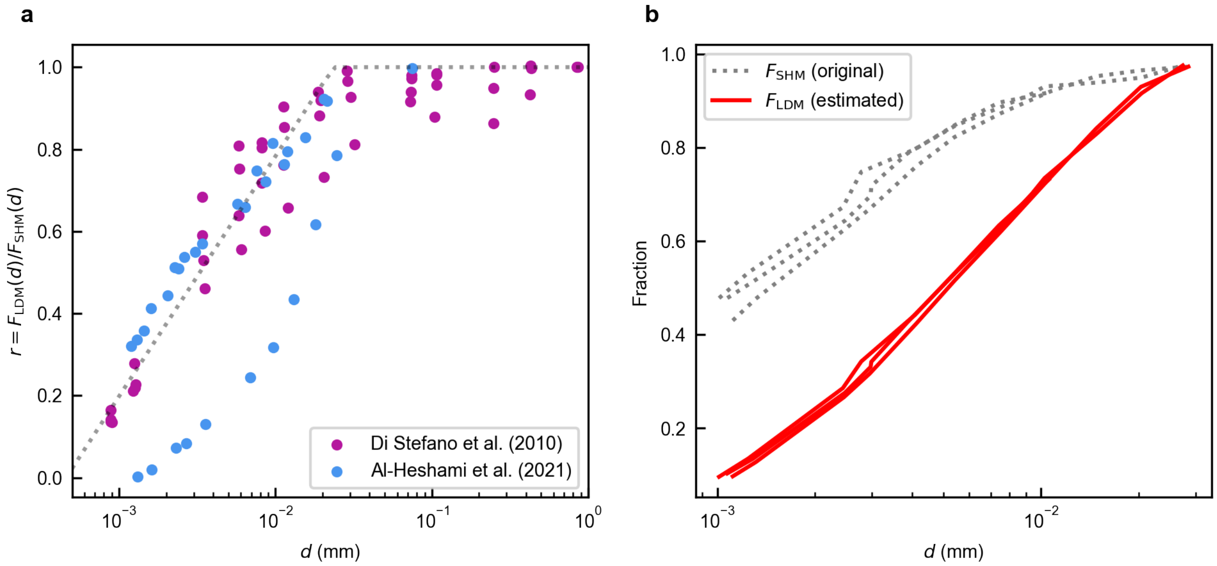

Figure S1. a) The ratio of particle sizes as measured by the Laser Diffraction method to that of the hydrometer analysis method. Gray dotted line represents the fitted curve. b) Modified particle-size distribution of Tesaker[4].

where d_i is the characteristic particle size of the i^{th} bin, N is the totall number of bins, and $f(d_i)$ denotes the fraction of the i^{th} particle size class which is given as

$$f(d_i) = \frac{q(d_i)}{\sum_k q(d_k)} \tag{S.11}$$

where $q(d_i)$ denotes the measured weight or volume of the particles in the i^{th} size bin. Let $r(d)$ denote the ratio of the cumulative fraction of particles measured by LDM to the one measured by SHM, such that

$$F_{\mathrm{LDM}}(d) = r(d) F_{\mathrm{SHM}}(d). \tag{S.12}$$

Figure S1a shows the calculated best fit function $r(d)$ from the compiled sources[30,31]; $r(d)$ increases monotonically as d increases until r reaches to unity at $d \simeq 3 \times 10^{-2}$.

Here, the relationship between r and $\log d$ for fine particles ($d < 3 \times 10^{-2}$) is approximated by the linear curve fitting with the least-square method (Gray dotted line in Fig. S1a). Then, assuming $r \leq 1$, the empirical formula of r is given as

$$r(d) = \min\left[a \log_{10} d + b, 1\right] \tag{S.13}$$

where the correlation coefficients are $a = 0.58 \pm 0.04$ and $b = 1.95 \pm 0.09$. Then, F_{LDM} of Tesaker's experiments[4] is estimated from the measured F_{SHM} by Equation (S.12) and (S.13) (Fig. S1b). Consequently, d_{50} shifted from around 1×10^{-3} mm to 4.98×10^{-3} on average (Fig. S1b). In the analysis of main text, 4.98×10^{-3} is used as the median particle size of Tesaker's experiments.

Extraction of original measurement points Depending on the availability of the dataset, different procedures were applied to extract data from the source. There were two cases: i) original raw measurement data (such as UVP measurements data) is available, ii) only figures of measured data points and interpolated and extrapolated profiles are available. In case (i), the raw data are directly used to reconstruct the flow profiles. In case (ii), the original measurements of vertical velocity and concentration are extracted by using a graph-read software (https://graphclick.en.softonic.com/mac). However, some of the sources have less than three points of velocity or concentration, which is not enough to apply the extrapolation method. Here, assuming that the potential errors due to the choice of interpolation and extrapolation near the maximum velocity height are relatively small, a few data points are manually added near the original data points along the interpolated curve in the original source.

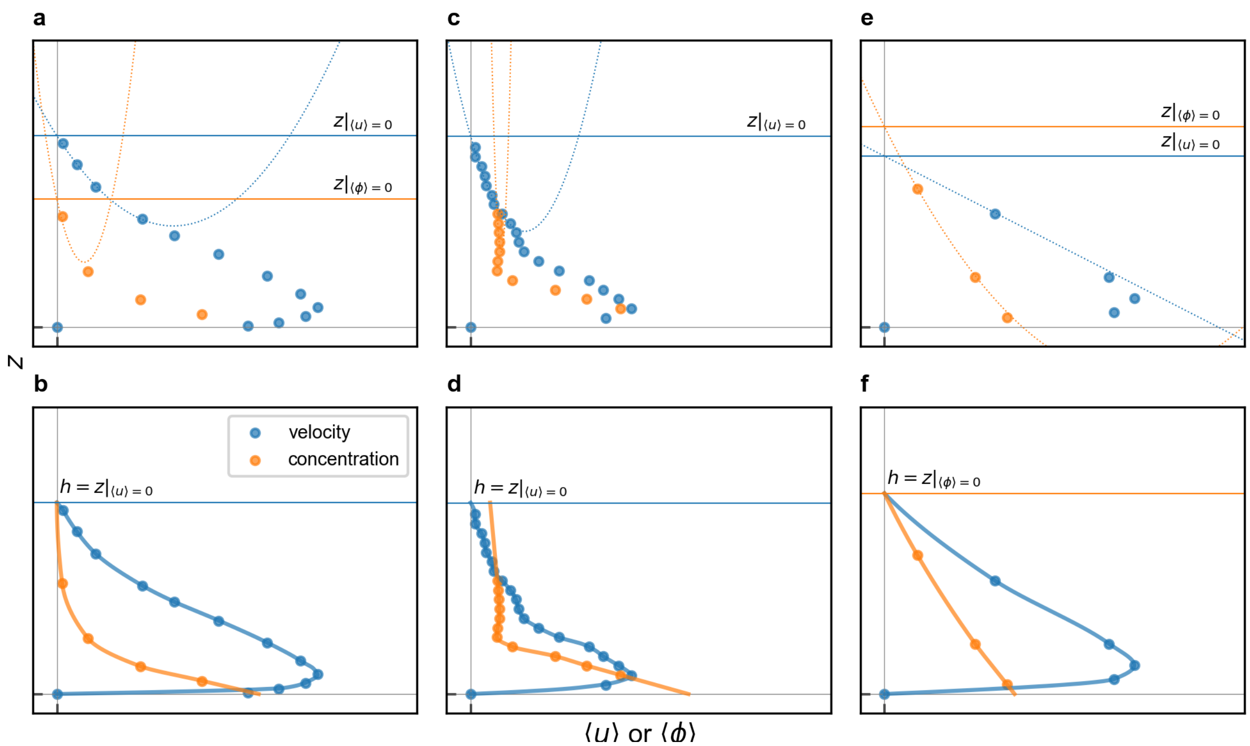

Figure S2. Schematic diagram of interpolation and extrapolation procedures for three different cases. Blue and orange markers represent the original measurement values. a) b) $z|_{\langle \phi \rangle = 0} < z_{u,n}$. c) d) $z|_{\langle u \rangle = 0} < z|_{\langle \phi \rangle = 0}$. e) f) $z_{u,n} < z|_{\langle \phi \rangle = 0} < z|_{\langle u \rangle = 0}$. a) c) e) Schematics of quadratic curve fitting for flow height estimation. Fitted curves are represented by dotted curves. b) d) f) Schematics of resultant flow profiles.

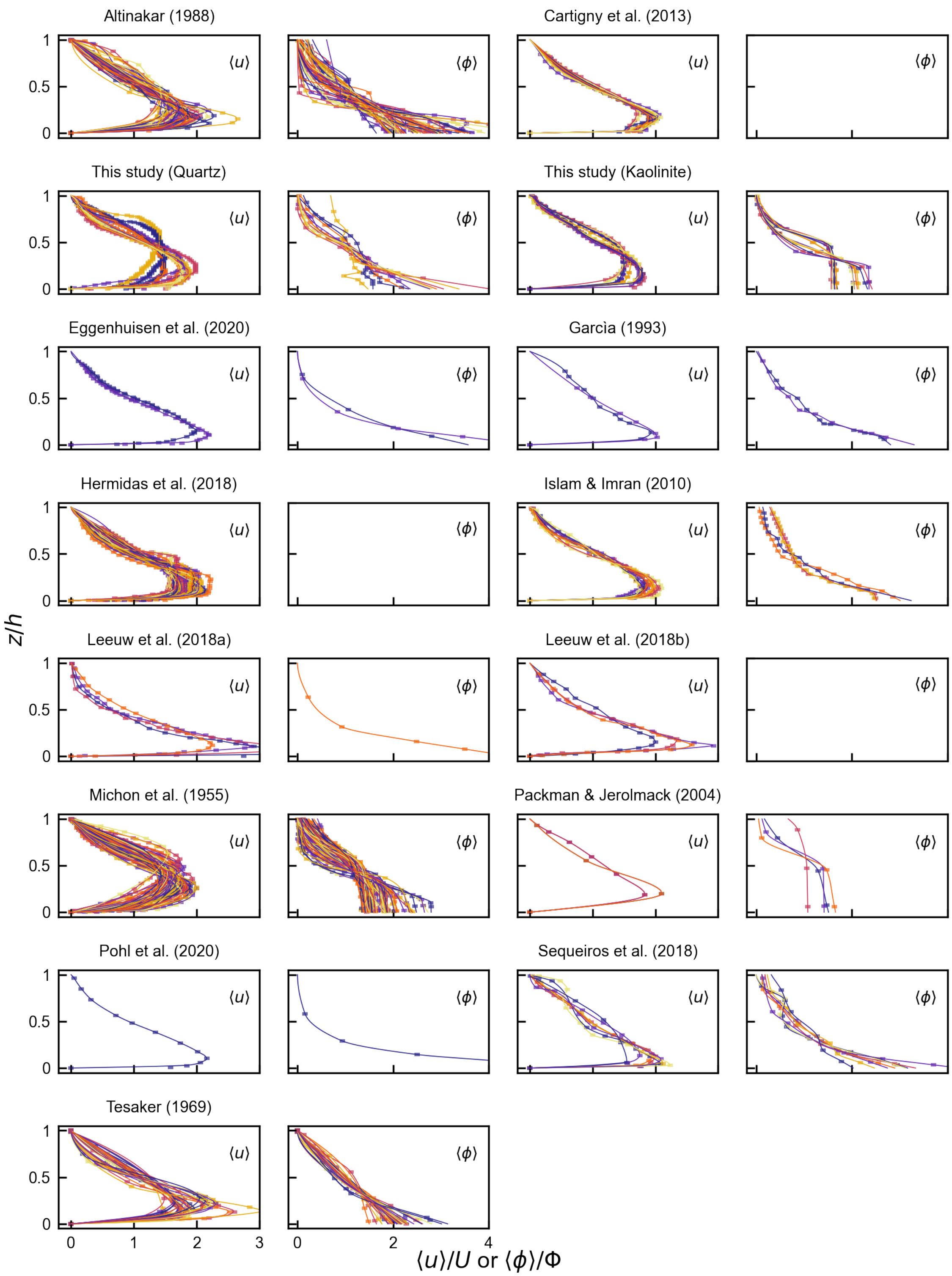

Figure S3. Interpolated and extrapolated flow profiles of the non-conservative flows from each source. For each source, velocity profiles are plotted on the left, and concentration profiles are on the right. X-axes are either flow velocity or flow concentration which is normalized by depth-averaged values, and Y-axes are the distance from the bed normalized by flow height.

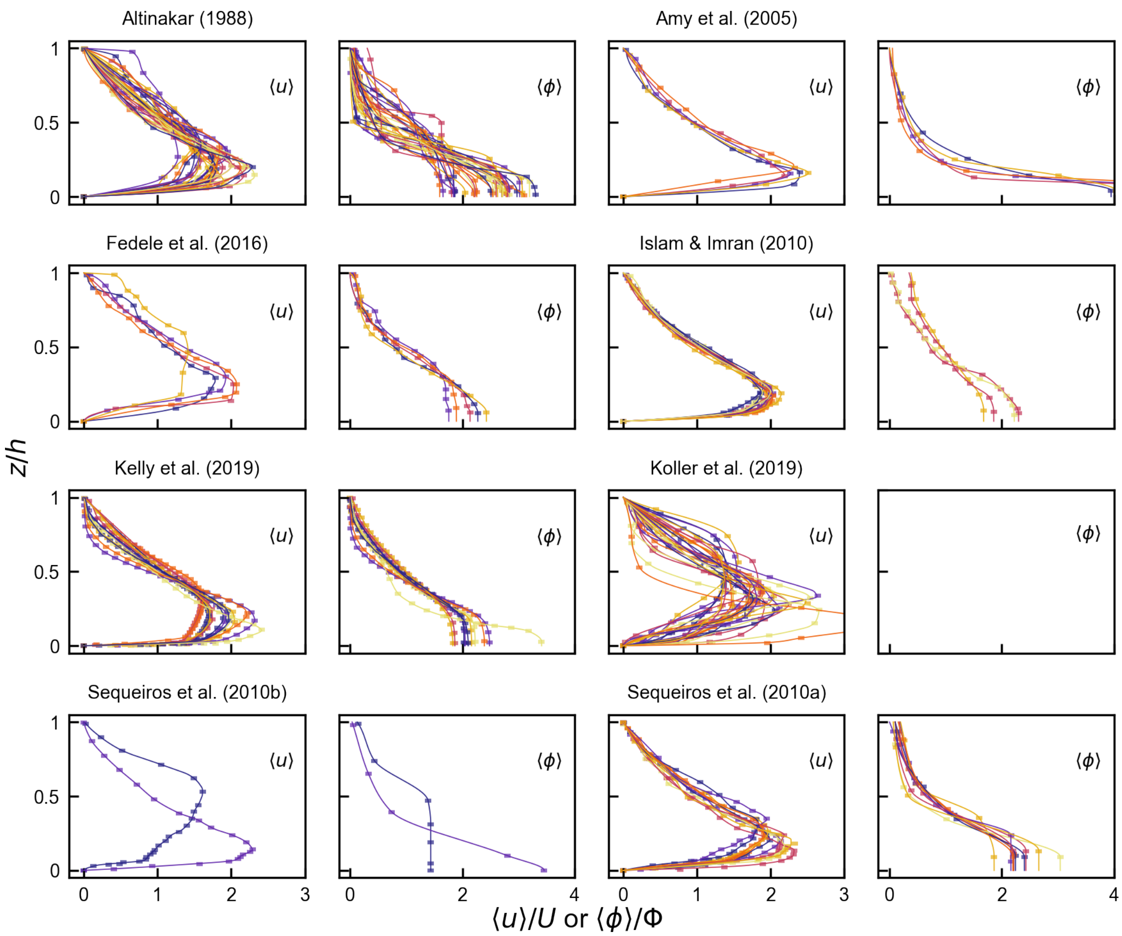

Figure S4. Interpolated and extrapolated flow profiles of the conservative flows from each source. For each source, velocity profiles are plotted on the left, and concentration profiles are on the right figure. X-axes are either flow velocity or flow concentration which is normalized by depth-averaged values, and Y-axes are the distance from the bed normalized by flow height.

Interpolation and extrapolation of flow profile The overall procedure can be summarized into three steps: i) data formatting, ii) estimation of flow height and near-bed concentration, and iii) interpolation and extrapolation. Details of each step are described in this section.

The first step is data formatting. Let $P_{\langle u\rangle} = \left[\mathbf{x}_{\langle u\rangle,1}, \mathbf{x}_{\langle u\rangle,2}, ...\mathbf{x}_{\langle u\rangle,n}\right]$ and $P_{\langle \phi\rangle} = \left[\mathbf{x}_{\langle \phi\rangle,1}, \mathbf{x}_{\langle \phi\rangle,2}, ...\mathbf{x}_{\langle \phi\rangle,m}\right]$ denote the extracted values of velocity and concentration. n and m denote the number of extracted measurement points of velocity and concentration respectively. $\mathbf{x}_{\langle u\rangle,i} = (\langle u\rangle|_{z=z_{u,i}}, z_{u,i})$ and $\mathbf{x}_{\langle \phi\rangle,i} = (\langle \phi\rangle|_{z=z_{\phi,i}}, z_{\phi,i})$ denote the i^{th} coordinate of extracted points. The data points are ordered from lowest to highest so that $z_i < z_{i+1}$. Thus, $z_{u,1}$ and $z_{\phi,1}$ are the lowest original measurement heights and $z_{u,n}$ and $z_{\phi,m}$ are the highest measurement heights. As boundary conditions, the following relationship is assumed for velocity profiles in this study.

$$\langle u\rangle|_{z=0} = \langle u\rangle|_{z=h} = 0, \tag{S.14}$$

To impose the lower boundary condition, an artificial data point $\mathbf{x}_{\langle u\rangle,0} = (0,0)$ is inserted into $P_{\langle u\rangle}$.

The next step is to estimate the flow height. The estimation of the flow height is performed in two steps: i) calculation of $z|_{\langle u\rangle=0}$ and $z|_{\langle \phi\rangle=0}$, and then ii) evaluation of flow height based on the comparison between $z|_{\langle u\rangle=0}$ and $z|_{\langle \phi\rangle=0}$. Firstly, interpolation of $P_{\langle u\rangle}$ and $P_{\langle \phi\rangle}$ is conducted using the PchipInterpolator function from Scipy, a Python package. This function provides a piecewise cubic Hermite interpolation[34]. One of the advantages of this interpolation method is that it does not overshoot even when the data is not smooth. Further, in this interpolation method, the original data points are always on the interpolated curve, which means that potential oversimplification is minimal. Let $f_{\langle u\rangle}(z)$ and $f_{\langle \phi\rangle}(z)$ denote the interpolated functions. Then, to obtain enough data points for processing, 500 vertically uniform data points are extracted from the interpolated function,

$$P_{f,\langle u\rangle} = \left[(f_{\langle u\rangle}(z_{fu,0}), z_{fu,0})...(f_{\langle u\rangle}(z_{fu,499}), z_{fu,499})\right], \;\; P_{f,\langle \phi\rangle} = \left[(f_{\langle \phi\rangle}(z_{f\phi,0}), z_{f\phi,0})...(f_{\langle \phi\rangle}(z_{f\phi,499}), z_{f\phi,499})\right]. \tag{S.15}$$

It should be noted that the points $(f_{\langle u\rangle}(z_{fu,499}), z_{fu,499})$ and $(f_{\langle \phi\rangle}(z_{f\phi,499}), z_{f\phi,499})$ correspond to the highest original data points, $\mathbf{x}_{\langle u\rangle,n}$ and $\mathbf{x}_{\langle \phi\rangle,m}$ respectively. Quadratic-function curve fitting is conducted against a upper part of the velocity profile to obtain $z|_{\langle u\rangle=0}$ and $z|_{\langle \phi\rangle=0}$ (Fig. S2a,c,e). For the velocity profile, the range of curve fitting is between $z_{fu,u_{\max}}$ and $z_{fu,499}$, where $z_{fu,u_{\max}}$ is the nearest data point to the velocity maximum. For the concentration profile, the range is between $z_{f\phi,249}$ and $z_{f\phi,499}$, where $z_{f\phi,249}$ denotes the data point at the middle height of interpolated region. The quadratic functionas, g_u and g_ϕ are given as,

$$g_u(u) = a_1\langle u\rangle^2 + a_2\langle u\rangle + a_3, \;\; g_\phi(\phi) = b_1\langle \phi\rangle^2 + b_2\langle \phi\rangle + b_3. \tag{S.16}$$

where (a_1, a_2, a_3) and (b_1, b_2, b_3) are the coefficients of best-fit curves estimated by the least-square method. The conditions, $a_1 > 0$ and $b_1 > 0$ are imposed to avoid unrealistic profile shapes. Then, $z|_{\langle u\rangle=0}$ and $z|_{\langle \phi\rangle=0}$ are obtained as,

$$z|_{\langle u\rangle=0} = g_u(0), \;\; z|_{\langle \phi\rangle=0} = g_\phi(\phi_{\text{ambient}}). \tag{S.17}$$

where ϕ_{ambient} is the concentration of the ambient fluid. Then, the flow height is given by,

$$h = \begin{cases} z|_{\langle u\rangle=0} & \text{when } z|_{\langle u\rangle=0} \le z|_{\langle \phi\rangle=0} \;\text{ or }\; z|_{\langle \phi\rangle=0} < z_{u,n}\;, \\ z|_{\langle \phi\rangle=0} & \text{when } z_{u,n} < z|_{\langle \phi\rangle=0} \le z|_{\langle u\rangle=0}. \end{cases} \tag{S.18}$$

$z|_{\langle \phi\rangle=0} < z_{u,n}$ sometimes happens when the number of data points in the density profile are inadequate. In this study, the original velocity measurements are regarded as more reliable than the extrapolated concentration curve. Thus, when $z|_{\langle \phi\rangle=0} < z_{u,n}$ (Fig. S2a,b), the extrapolation of the concentration profile is discarded and $h = z|_{\langle u\rangle=0}$ is the flow depth. Then, a new velocity point at the top of the flow $\mathbf{x}_{\langle u\rangle,h} = (0,h)$ is inserted into P_u. For the concentration profile, the value of the concentration at the flow height, $\mathbf{x}_{\langle \phi\rangle,h}$ is not necessarily always ϕ_{ambient}. When $z|_{\langle u\rangle=0} \le z|_{\langle \phi\rangle=0}$, the flow concentration at the flow height is estiamted by a piecewise cubic Hermite interpolation of original measurement points with $(0, z|_{\langle \phi\rangle=0})$. Let $f'_\phi(z)$ denote the interpolated function. Then, the flow concentration at the flow height is given as $f'_{\langle \phi\rangle}(z=h)$.

The final step is the interpolation and extrapolation of the rest of the profiles. Extrapolation is required to estimate the near-bed concentration, $\langle \phi\rangle_{\text{bed}}$. For the non-conservative currents, the first-order polynomial curve fit is conducted against the lowest two data points. For the conservative flow, the lowest original measurement point $\langle \phi\rangle|_{z=z_{\phi,0}}$ is used as the near-bed concentration. Then, combining the original measurements points, near-bed points, and flow height points, the following completed data lists were obtained,

$$P'_{\langle u\rangle} = \left[\mathbf{x}_{\langle u\rangle,\text{bed}}, \mathbf{x}_{\langle u\rangle,1}, ...\mathbf{x}_{\langle u\rangle,n}, \mathbf{x}_{\langle u\rangle,h}\right], \;\; P'_{\langle \phi\rangle} = \left[\mathbf{x}_{\langle \phi\rangle,\text{bed}}, \mathbf{x}_{\langle \phi\rangle,1}, ...\mathbf{x}_{\langle \phi\rangle,m}, \mathbf{x}_{\langle \phi\rangle,h}\right]. \tag{S.19}$$

Finally, by conducting piecewise cubic Hermite interpolation against $P'_{\langle u\rangle}$ and $P'_{\langle \phi\rangle}$, the full profile $\langle u\rangle(z)$ and $\langle \phi\rangle(z)$ were obtained. The full profiles for each source obtained by the methodology described here are plotted in Figure S3, S4, and S6.

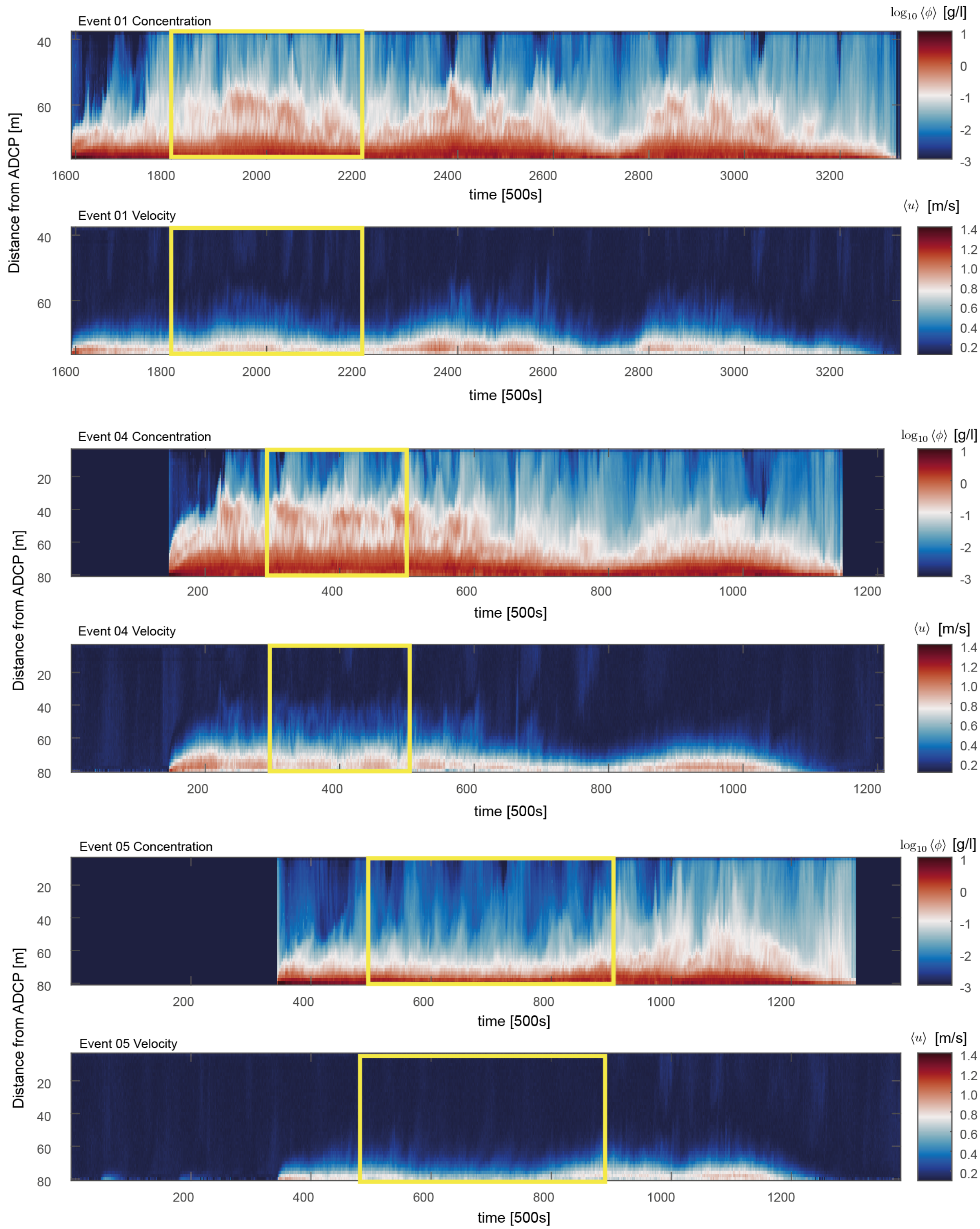

Figure S5. Time series of velocity and concentration structures of Congo's event. The selected time window is depicted with yellow rectangles.

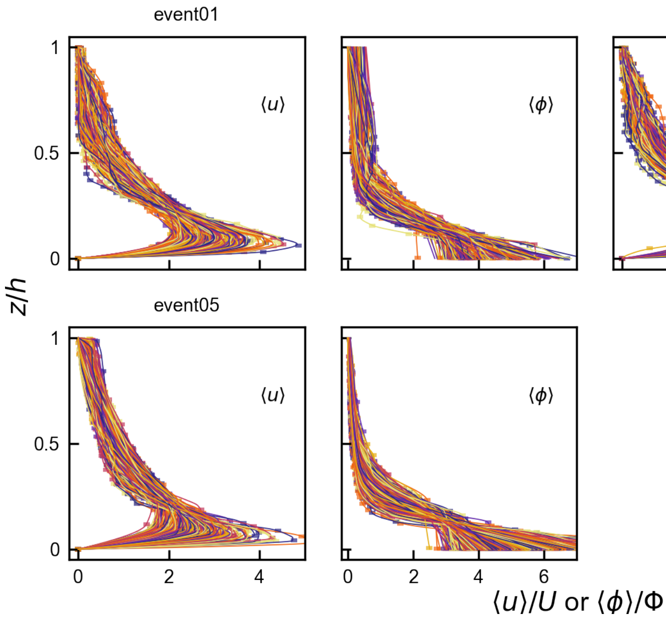

Figure S6. Time-averaged vertical profiles of each event. Each profile is 500 seconds time-averaged profile from a steady part of each event.

Turbidity currents from Congo canyon The real-world dataset (TYPE I in the main text) from Congo canyon is extracted from the source of direct measurements[22]. In Simmons et al.[22], flow velocity and concentration structures are measured by Acoustic Doppler Current Profilers (ADCPs). In this study, to investigate the flow dynamics of quasi-equilibrium natural-scale turbidity currents, relatively long-duration (more than 5 days) events are chosen (Event 01, 04, and 05). Some long-duration events in which velocity and concentration fields drastically changed during the flow event (such as Events 8, 9, and 10 from the original source) are excluded.

From each event, intervals of time are selected so that the compiled dataset does not include the head and tail parts of each event (Fig. S5). To remove the background noise from each flow, the time-average background velocity is calculated for each run. Then the region where the velocity values were lower than twice the time-averaged background noise is excluded in the interpolation and extrapolation of profiles. Then, the relative velocity against the time-averaged background velocity is extracted as the flow velocity measurements.

The original concentration profiles include some artifacts[22]. In events 1 and 4, sometimes concentration values suddenly increase near the interface with the ambient. Simmons et al.[22] assumed that this type of artifact is presumably related to the backscatter from turbulent microstructure associated with gradients in either density, temperature, or salinity[35]. To exclude the artifacts, the peak value of the concentration near the upper flow interface is measured from Event 1 and 4. Then, in the upper half of the flow, the concentration lower than this peak is omitted; only the portion of the concentration data which is of higher concentration than the artifact is used for interpolation and extrapolation. Then, the extrapolation method detailed above is applied to recover the full profiles (Fig. S6).

Estimation of depth-averaged concentration To estimate the depth-averaged sediment concentration, Φ, for the experiments in which the vertical concentration profiles are not available (TYPE III, see Table S1), the following empirical relationship between Φ and the initial sediment concentration in the mixing tank, Φ_0 are deduced, using orthogonal distance regression, from TYPE II data where the both parameters are available (Fig. S7). Then, Φ of TYPE III data is assumed to follow the obtained empirical formula,

$$\Phi \simeq 0.30 \times {\Phi_0}^{0.94} \tag{S.20}$$

Flume Experiments

The experiments are carried out in the flume laboratory in the Total Environmental Simulator at The DEEP. The flow properties (Table 1 in the main text) are chosen to fill the gaps between the data points from the compiled sources (Fig. S8). A schematic

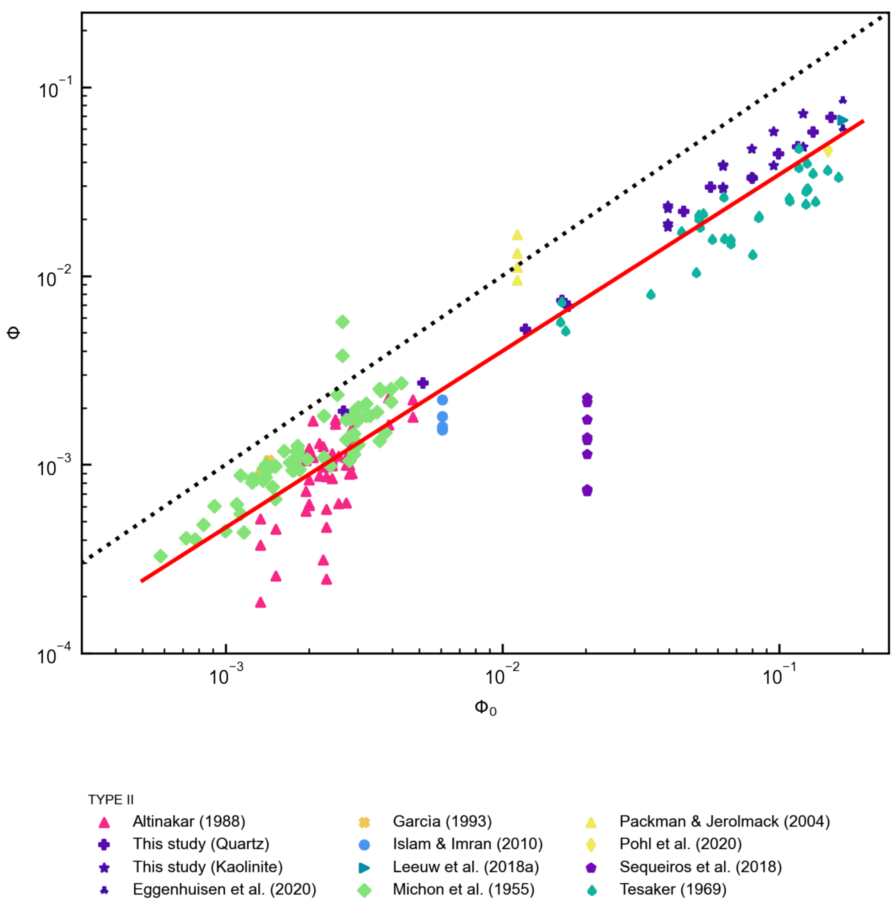

Figure S7. Log-log plot of layer-averaged flow concentration and initial concentration of the sediment-water mixture in the mixing tank of each experiment. The regression line (gray dotted line) was fitted to logarithmic values of Φ_0 and Φ. The coefficient of determination is $R = 0.88$.

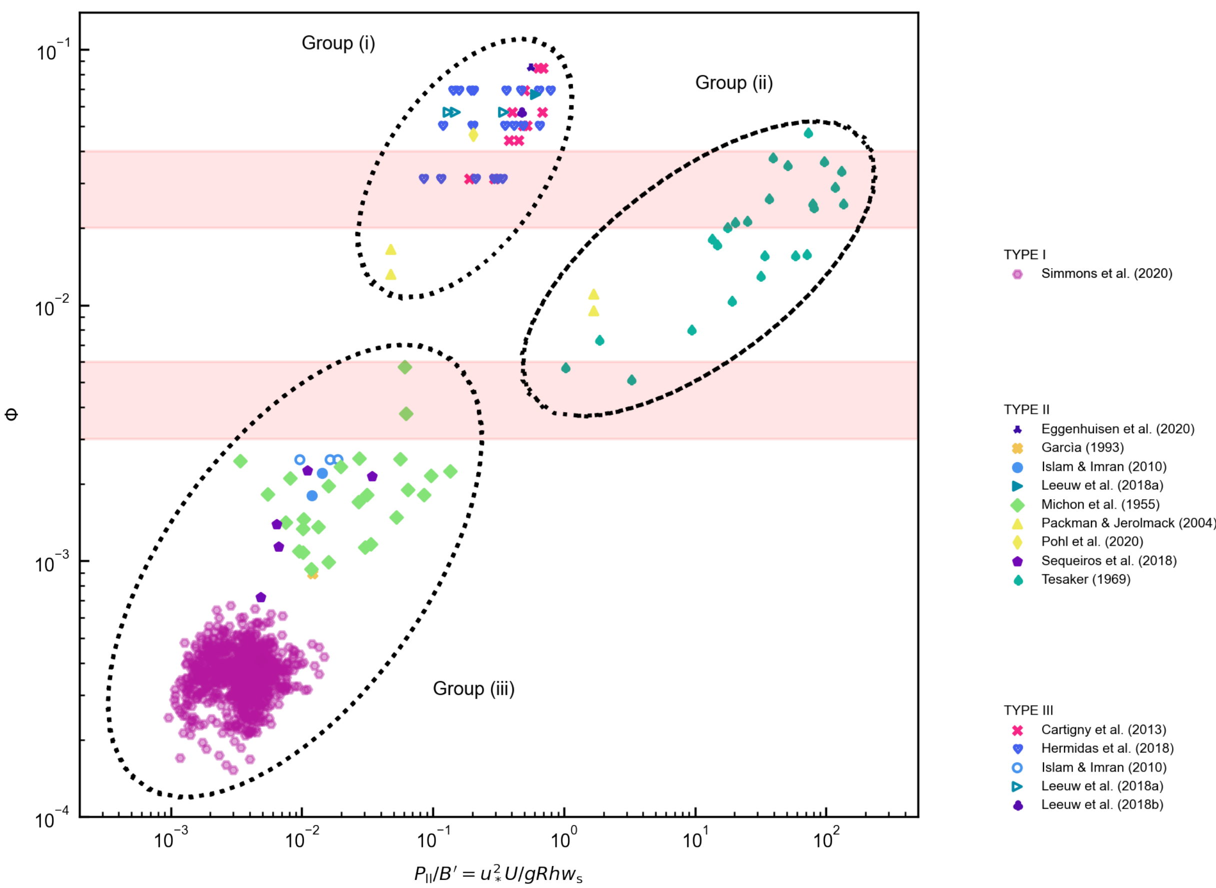

Figure S8. Flow power plot with target flow concentration regions (red shaded area) of the flume experiments. Part of the experiments was aimed at filling the gap between groups of data points (i) and (ii). The rest of the experiments were aimed to supply the data between the group (ii) and (iii).

and description of the experimental settings is given in the main text (Fig. 6 in the main text). Here, the preparation of the sediment-water mixture and bed profile measurement which is conducted to measure the aggradation rate are elaborated.

Preparation of sediment-water mixture A large corn-shape mixing tank is built and used to generate turbidity currents (in total 1.36 m^3 including the region below the mixer which cannot be used; the total effective volume for the experimental run above the mixer is approximately 0.97 m^3). To keep the concentration vertically uniform, two different mixing systems are established: i) an electrical mixer with a set of 350 mm diameter impellers is inserted from the top of the tank which generates a strong vortex within the tank, and 2) a re-circulation piping system with a pump is connected from the bottom of the tank to the top of the tank which generates vertical circulation. Another piping system is connected with a slurry pump (Ebara DWO 300) from the fit on the sidewall of the tank to the flow diffuser inserted upstream of the perspex straight channel. The (pumped) input rate is tested by adjusting the in-line valve, reading the flow rate from an electromagnetic flowmeter during test runs. The sediment concentration in the mixing tank and in each flow are calculated from the wet and dry weight of collected samples. Finally, the dry sample was analyzed by a laser particle sizer (Malvern Mastersizer) to estimate the detailed particle size distribution.

Bed profile Aggradation rate, for flow equilibrium, and bed depth is monitored by using the bed profiler from a single ADV (Acoustic Doppler Velocimeter) suspended above the flow. In addition to the ADV, 4 ultrasonic sensors (URSs) to monitor the aggradation rate are mounted. To reduce mobile bedload, and ADV measurement noise, experiments start with the unerodible bed of the Perspex channel. The maximum aggradation rate of the well-developed flow body observed in our experiments is 0.1 mm/s in run 11. It should be noted that for high concentrated runs (experiments 01–07 and 13–17, see Table 2 in the main text) both ADV and URSs failed to monitor the bed height during the flow events. For those runs, the aggradation rate is monitored from the videos that were captured by high-resolution GoPro cameras. As result, for those high concentration runs, deposition only occurred at the very end of the flow event (the tail of the flow) but we observed almost no deposition from the head and body of each flow where the velocity and density measurement are conducted.

Flow power plot

The empirical relationship of this study takes the following form:

$$\log\Phi = a\log\left(\frac{u_*^2U}{gRhw_s}\right) + \log b, \tag{S.21}$$

where $a \simeq 0.46$ and $b \simeq 5.2\times10^{-3}$ are the constants which are estimated by the orthogonal distance regression analysis. Equation (S.21) can be readily rewritten as

$$\Phi = b\left(\frac{u_*^2U}{gRhw_s}\right)^a \tag{S.22}$$

Congo's data Congo's turbidity current data[22] (TYPE I) show a wide range of the power ratio, λ (Fig. S10a). Overall flow power relation (Eq. S.21) show a good agreement with the trend with Experimental flows in Figure. 3 in the main text. Here the sensitivity of the fit parameters, a and b against λ, are examined by applying various power ratio threshold ($1/\lambda_c < \lambda < \lambda_c$, see Fig. S9). Overall, the fit parameters show almost constant values ($0.4 \lesssim a \lesssim 0.5$ and $0.3\times10^{-2} \lesssim b \lesssim 0.5\times10^{-2}$) regardless of λ_c. The regression curve of TYPE I data with $\lambda_C = 5/4$ shows $a \simeq 0.46$ and $b \simeq 4.0\times10^{-3}$ ($R^2 = 0.58$) (Fig. S10b).

Curve Fitting

In the main text, two types of regression analyses are conducted. For the simple linear regression, orthogonal distance regression (ODR) method[36] is used. For the curve fittings of the non-linear correlation between dimensionless flow power and the flow concentration in Figure 4a,b in the main text, a least square method was applied with quadratic and cubic functions. In this section, the detailed methods of curve fitting is elaborated.

Flow power plot To fit a curve to the data in figure 4a,b in the main text, we use a least squares fit for a parametric curve fitting. To simplify notation, here we will use the notation $x = \log_{10}(u_\star^2U/Rghw_s)$, $y = \log_{10}(\Phi)$ so that the goal is to fit a curve $(x(t), y(t))$ to the given set of data points (x_i, y_i). The curves are written as polynomials in the parameter t, and we choose to take x as a quadratic in t and y as a cubic in t, so that

$$x = \sum_{n=0}^{2} a_n t^n, \qquad y = \sum_{n=0}^{3} b_n t^n. \tag{S.23}$$

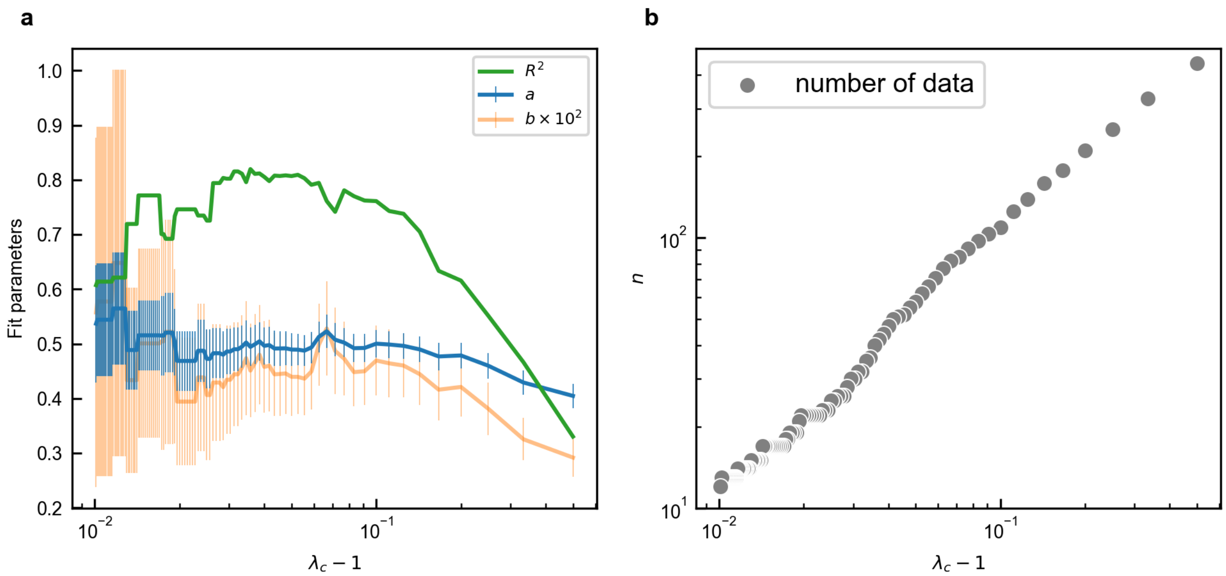

Figure S9. λ_c dependency of the fit parameters of Equation (S.22) of TYPE I data. a) Fit parameters, a and b, versus power ratio threshold, λ_c. Error bars are indicated by the vertical lines. b) Sample size, n, versus power ratio threshold λ_c.

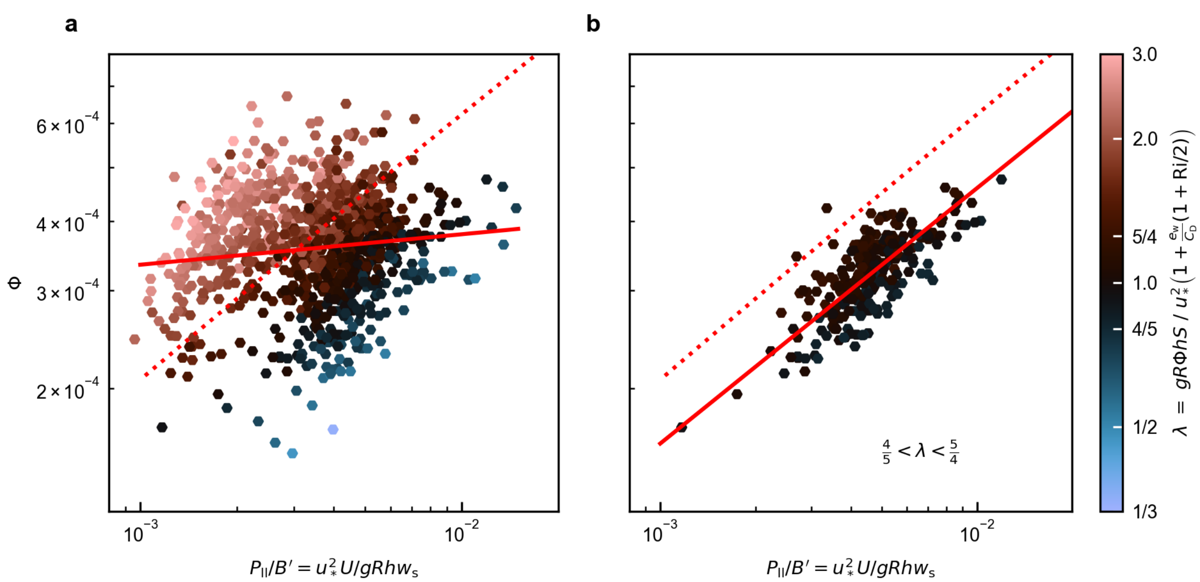

Figure S10. Sediment transport capacity for Congo's turbidity currents. a) Sediment concentration, Φ, versus dimensionless flow power, P_{ll}/B' from TYPE I data[22]. Color represents the power ratio, λ. b) Refined data points where $4/5 < \lambda < 5/4$. Red solid line is a fitted curve by ODR. Red dotted line is the regression curve fitted to the all data points by iterative least-square methods in the Figure 3 in the main text.

This parametrization in the variable t has a symmetry of the form $t \mapsto c_0 + c_1 t$, which has corresponding transformations for the coefficients a_n, b_n, that keeps the curve in the x-y plane unchanged. To remove this symmetry, we select two of the coefficients by choosing $t = 0$ to correspond to the extrenal value of x, $a_1 = 0$, and the rate of change of y around this point to be unity, $b_1 = 1$.

To fit the curve to the data (x_i, y_i), we recognise that we must not only determine the coefficients a_n, b_n, but also a set of values t_i which are the parameter values for the closest point on the curve to the data point. We do this employing the residuals

$$\varepsilon_i(\boldsymbol{\beta}) = x_i - f_i(\boldsymbol{\beta}) \qquad \text{where} \qquad f_i(\boldsymbol{\beta}) = \sum_{n=0}^{2} a_n t_i^n, \tag{S.24}$$

and

$$\delta_i(\boldsymbol{\beta}) = y_i - g_i(\boldsymbol{\beta}) \qquad \text{where} \qquad g_i(\boldsymbol{\beta}) = \sum_{m=0}^{3} b_n t_i^m, \tag{S.25}$$

where bold characters denote column vectors or matrices, and $\boldsymbol{\beta}$ will be defined later. For now we simply state it is the value to be optimised. The sum of squared residuals is then

$$S(\boldsymbol{\beta}) = \sum_i (\varepsilon_i(\boldsymbol{\beta})^2 + \delta_i(\boldsymbol{\beta})^2). \tag{S.26}$$

and we employ the method of least squares, seeking a local minimum of $S(\boldsymbol{\beta})$. Following the standard deviation for the method of least squares, we can find a local minimum by iterating from one value, $\boldsymbol{\beta}^k$, to the next, $\boldsymbol{\beta}^{k+1}$, using

$$(\boldsymbol{F}^T\boldsymbol{F} + \boldsymbol{G}^T\boldsymbol{G})\Delta\boldsymbol{\beta} = \boldsymbol{F}^T\boldsymbol{\varepsilon} + \boldsymbol{G}^T\boldsymbol{\delta} \tag{S.27}$$

where $\boldsymbol{\beta}^{k+1} = \boldsymbol{\beta}^k + \Delta\boldsymbol{\beta}$ and

$$F_{ij} = \frac{\partial f_i}{\partial \beta_j}(\boldsymbol{\beta}^k), \qquad G_{ij} = \frac{\partial g_i}{\partial \beta_j}(\boldsymbol{\beta}^k). \tag{S.28}$$

The algorithm we use proceeds as follows, where $\|\boldsymbol{\beta}\| = \frac{1}{M}\sum_{m=1}^{M} \beta_m$.

1. Initialise the values of t_i to $t_i = 1$ for $x_i < 1$, $y_i > -2$; to $t_i = 0$ for $x_i \geq 1$; and to $t_i = -1$ otherwise. Add to these t_i a random amount between -0.05 and 0.05 to desingularize what follows.
2. Initialise a_n and b_n to random values between 0 and 1, except for $a_1 = 0$ and $b_1 = 1$.
3. Apply the iteration S.27 with $\boldsymbol{\beta} = (a_0, a_2, b_0)^T$ until $\|\Delta\boldsymbol{\beta}\| < 10^{-4}$, which is equivalent to fitting x as a quadratic in y,
4. Apply the iteration S.27 with $\boldsymbol{\beta} = (a_0, a_2, b_0, b_2, b_3, t_0, t_1, \ldots)^T$ and $\boldsymbol{\beta}^{k+1} = \boldsymbol{\beta}^k + \frac{1}{10}\Delta\boldsymbol{\beta}$ until $\|\Delta\boldsymbol{\beta}\| < 10^{-4}$, which is the full fitting of the curve
5. For points with $x_i \geq 1$, search over values of t to find a t_i that is the global minimizer of $\varepsilon_i^2 + \delta_i^2$, to ensure that all data points are identified with the correct points on the curve
6. Apply step 4 again

At this stage, the resulting $y(t)$ is not monotone for either the fluvial or turbidity current data, and consequently x cannot be considered a (single valued) function of y. To remedy this problem we first note that the minimal value of $\mathrm{d}y/\mathrm{d}t$ occurs at the inflection point $t = -b_2/3b_3$, and takes the value $b_1 - b_2^2/3b_3$. Using that $b_1 = 1$, we set $b_3 = b_2^2/3$, and then proceed as follows

7. Apply the iteration S.27 with $\boldsymbol{\beta} = (a_0, a_2, b_0, b_2, t_0, t_1, \ldots)^T$ and $\boldsymbol{\beta}^{k+1} = \boldsymbol{\beta}^k + \frac{1}{10}\Delta\boldsymbol{\beta}$ until $\|\Delta\boldsymbol{\beta}\| < 10^{-4}$
8. Apply step 5 again
9. Apply step 7 again

At this stage the optimal values of a_n and b_n are known, and can be used to plot the best fit curve. For both cases $a_1 = 0$, $b_1 = 1$, and $b_3 = b_2^2/3$. For the fluvial case

$$a_0 = 0.663, \qquad a_2 = -1.17, \qquad b_0 = -1.32, \qquad b_2 = -0.483, \qquad -1.40 < t < 1.27. \tag{S.29}$$

For the turbidity current case

$$a_0 = 2.14, \qquad a_2 = -35.7, \qquad b_0 = -1.42, \qquad b_2 = -6.96, \qquad -0.379 < t < 0.299. \tag{S.30}$$

References

1. Pope, S. B. & Pope, S. B. *Turbulent flows* (Cambridge university press, 2000).
2. Michon, X., Goddet, J. & Bonnefille, R. *Etude theorique et experimentale des courants de densite* (Laboratoire national d'hydraulique, 1955).
3. Altinakar, M. S. *Weakly Depositing Turbidity Currents on Small Slopes*. PhD dissertation, EPF Lausanne, CH. (1988).
4. Tesaker, E. *Uniform turbidity current experiments*. PhD dissertation, The Technical University of Norway (1969).
5. Soulsby, R. *Dynamics of marine sands* (T. Telford London, 1997).
6. Garcìa, M. H. Hydraulic jumps in sediment-driven bottom currents. *J. Hydraul. Eng.* **119**, 1094–1117, DOI: 10.1061/(ASCE)0733-9429(1993)119:10(1094) (1993).
7. Packman, A. & Jerolmack, D. The role of physicochemical processes in controlling sediment transport and deposition in turbidity currents. *Mar. Geol.* **204**, 1–9, DOI: 10.1016/S0025-3227(03)00359-1 (2004).
8. Amy, L., Peakall, J. & Talling, P. Density- and viscosity-stratified gravity currents: Insight from laboratory experiments and implications for submarine flow deposits. *Sedimentary Geol.* **179**, 5 – 29, DOI: 10.1016/j.sedgeo.2005.04.009 (2005). Sedimentary Gravity Flows: Recent Advances in Process and Field Analysis.
9. Islam, M. A. & Imran, J. Vertical structure of continuous release saline and turbidity currents. *J. Geophys. Res. Ocean.* **115**, DOI: 10.1029/2009JC005365 (2010).
10. Sequeiros, O. E. *et al.* Bedload transport and bed resistance associated with density and turbidity currents. *Sedimentology* **57**, 1463–1490, DOI: 10.1111/j.1365-3091.2010.01152.x (2010).
11. Sequeiros, O. E. *et al.* Characteristics of velocity and excess density profiles of saline underflows and turbidity currents flowing over a mobile bed. *J. Hydraul. Eng.* **136**, 412–433, DOI: 10.1061/(ASCE)HY.1943-7900.0000200 (2010).
12. Cartigny, M. J., Eggenhuisen, J. T., Hansen, E. W. & Postma, G. Concentration-dependent flow stratification in experimental high-density turbidity currents and their relevance to turbidite facies models. *J. Sedimentary Res.* **83**, 1047–1065, DOI: 10.2110/jsr.2013.71 (2013).
13. Fedele, J. J., Hoyal, D., Barnaal, Z., Tulenko, J. & Awalt, S. Bedforms created by gravity flows. In *Autogenic Dynamics and Self-Organization in Sedimentary Systems*, DOI: 10.2110/sepmsp.106.12 (SEPM Society for Sedimentary Geology, 2016).
14. de Leeuw, J., Eggenhuisen, J. T. & Cartigny, M. J. B. Linking submarine channel–levee facies and architecture to flow structure of turbidity currents: insights from flume tank experiments. *Sedimentology* **65**, 931–951, DOI: https://doi.org/10.1111/sed.12411 (2018).
15. de Leeuw, J. *et al.* Sediment volume and grain-size partitioning between submarine channel-levee systems and lobes: An experimental study. *J. Sedimentary Res.* **88**, 777–794, DOI: 10.2110/jsr.2018.46 (2018).
16. Hermidas, N. *et al.* A classification of clay-rich subaqueous density flow structures. *J. Geophys. Res. Earth Surf.* **123**, 945–966, DOI: 10.1002/2017JF004386 (2018).
17. Sequeiros, O. E., Mosquera, R. & Pedocchi, F. Internal structure of a self-accelerating turbidity current. *J. Geophys. Res. Ocean.* **123**, 6260–6276, DOI: 10.1029/2018JC014061 (2018).
18. Eggenhuisen, J. T., Tilston, M. C., de Leeuw, J., Pohl, F. & Cartigny, M. J. B. Turbulent diffusion modelling of sediment in turbidity currents: An experimental validation of the rouse approach. *The Depositional Rec.* (2019).
19. Kelly, R. W., Dorrell, R. M., Burns, A. D. & McCaffrey, W. D. The structure and entrainment characteristics of partially confined gravity currents. *J. Geophys. Res. Ocean.* **124**, 2110–2125, DOI: 10.1029/2018JC014042 (2019).
20. Koller, D., Manica, R., Borges, A. d. O. & Fedele, J. Experimental bedforms by saline density currents. *Brazilian Journal of Geology* **49**, DOI: 10.1590/2317-4889201920180118 (2019).
21. Pohl, F., Eggenhuisen, J. T., Kane, I. A. & Clare, M. A. Transport and burial of microplastics in deep-marine sediments by turbidity currents. *Environ. Sci. & Technol.* **54**, 4180–4189, DOI: 10.1021/acs.est.9b07527 (2020).
22. Simmons, S. M. *et al.* Novel acoustic method provides first detailed measurements of sediment concentration structure within submarine turbidity currents. *J. Geophys. Res. Ocean.* **125**, e2019JC015904, DOI: 10.1029/2019JC015904 (2020).
23. Fisher, P., Aumann, C., Chia, K., O'Halloran, N. & Chandra, S. Adequacy of laser diffraction for soil particle size analysis. *PLOS ONE* **12**, 1–20, DOI: 10.1371/journal.pone.0176510 (2017).

24. Goossens, D. Techniques to measure grain-size distributions of loamy sediments: a comparative study of ten instruments for wet analysis. *Sedimentology* **55**, 65–96, DOI: 10.1111/j.1365-3091.2007.00893.x (2008).

25. Eshel, G., Levy, G. J., Mingelgrin, U. & Singer, M. J. Critical evaluation of the use of laser diffraction for particle-size distribution analysis. *Soil Sci. Soc. Am. J.* **68**, 736–743, DOI: 10.2136/sssaj2004.7360 (2004).

26. Katayama, H. Comparison between a lazer diffraction-scattering method and a hydrometer method in the grain size analysis for fine-grained sediments. *J. Sedimentol. Soc. Jpn.* **46**, 23–30, DOI: 10.4096/jssj1995.46.23 (1997).

27. Vitton, S. J. & Sadler, L. Y. Particle-size analysis of soils using laser light scattering and x-ray absorption technology. *Geotech. Test. J.* **20**, 63–73 (1997).

28. Konert, M. & Vandenberghe, J. Comparison of laser grain size analysis with pipette and sieve analysis: a solution for the underestimation of the clay fraction. *Sedimentology* **44**, 523–535, DOI: 10.1046/j.1365-3091.1997.d01-38.x (1997).

29. Lu, N., Ristow, G. H. & Likos, W. J. The accuracy of hydrometer analysis for fine-grained clay particles. *Geotech. Test. J.* **23**, 487–495 (2000).

30. Di Stefano, C., Ferro, V. & Mirabile, S. Comparison between grain-size analyses using laser diffraction and sedimentation methods. *Biosyst. Eng.* **106**, 205–215, DOI: 10.1016/j.biosystemseng.2010.03.013 (2010).

31. Al-Hashemi, H. M. B., Al-Amoudi, O. S. B., Yamani, Z. H., Mustafa, Y. M. & Ahmed, H.-u.-R. The validity of laser diffraction system to reproduce hydrometer results for grain size analysis in geotechnical applications. *PLOS ONE* **16**, 1–18, DOI: 10.1371/journal.pone.0245452 (2021).

32. Lopez, A., Gustavsson, H. & Korkiala-Tanttu, L. Comparison between hydrometer and laser diffraction methods in the determination of clay content in fine-grained soils. *IOP Conf. Series: Earth Environ. Sci.* **710**, 012012, DOI: 10.1088/1755-1315/710/1/012012 (2021).

33. Bah, A. R., Kravchuk, O. & Kirchhof, G. Fitting performance of particle-size distribution models on data derived by conventional and laser diffraction techniques. *Soil Sci. Soc. Am. J.* **73**, 1101–1107, DOI: 10.2136/sssaj2007.0433 (2009).

34. Fritsch, F. N. & Butland, J. A method for constructing local monotone piecewise cubic interpolants. *SIAM J. on Sci. Stat. Comput.* **5**, 300–304, DOI: 10.1137/0905021 (1984).

35. Lavery, A. C., Schmitt, R. W. & Stanton, T. K. High-frequency acoustic scattering from turbulent oceanic microstructure: The importance of density fluctuations. *The J. Acoust. Soc. Am.* **114**, 2685–2697, DOI: 10.1121/1.1614258 (2003).

36. Boggs, P. T. & Rogers, J. E. Orthogonal distance regression. *Contemp. Math.* **112**, 183–194 (1990).